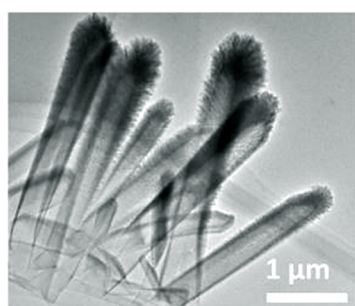
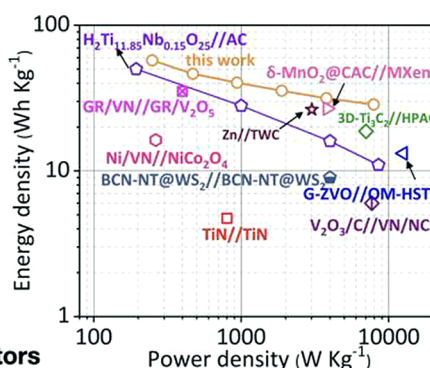


# Bimetallic Nitride TiVN Hollow Nanotubes for High-Performance Zinc-Ion Hybrid Supercapacitors

Hao Zhou, Zhilong Zheng, Huanhuan Shi,<sup>\*</sup> Jiaxian Zheng, Yuwei Zhang, Weijie Zhu, Fangwang Ming,<sup>\*</sup> Zhoucheng Wang, and Hanfeng Liang<sup>\*</sup>



**Hollow TiVN for Zn-ion Capacitors**



**ABSTRACT:** Zinc-ion hybrid supercapacitors (ZIHCs) hold great promise in the realm of renewable energy storage. However, their development is severely hampered by the unsatisfactory practical capacity and poor stability. Herein, we report an effective strategy to improve the electrochemical performance by constructing hollow bimetallic nitride TiVN (H-TiVN) using a sacrificial template method. The optimized H-TiVN//Zn shows a high capacitance of 183.7 F g<sup>-1</sup> at 0.2 A g<sup>-1</sup> along with excellent stability (an 84.7% capacitance retention after 20,000 cycles at 5 A g<sup>-1</sup>). More importantly, the energy density can reach 57.42 Wh kg<sup>-1</sup>, accompanied by a power density of 249.35 W kg<sup>-1</sup>. Our work not only establishes H-TiVN as a high-performance electrode material for ZIHCs but also provides a general strategy for improving the electrochemical performance of nanomaterial electrodes.

Hybrid supercapacitors, which are composed of battery-type (faradaic) electrodes and capacitor-type (nonfaradaic) electrodes, combine the merits of high energy density of the former and high power density of the latter and therefore are of significant research and practical interest. Over the past few years, hybrid supercapacitors using Li<sup>+</sup>, Na<sup>+</sup>, K<sup>+</sup>, Ca<sup>2+</sup>, Mg<sup>2+</sup>, and Zn<sup>2+</sup> as the charge carriers have been widely investigated.<sup>1–3</sup> Among them, zinc-ion hybrid supercapacitors (ZIHCs) stand out given their high safety, low cost, and high energy/power density. The ZIHC directly utilizes Zn foil as the battery-type electrode, which possesses a high theoretical capacity (819 mAh g<sup>-1</sup> or 5854 mAh cm<sup>-3</sup>), excellent electrical conductivity, and suitable redox potential (−0.76 V versus the standard hydrogen electrode).<sup>4–8</sup> Carbon materials are the most studied capacitor-type electrodes; however, they are limited by their relatively low capacitance. Though tremendous efforts have been devoted to improving the performance of carbon electrodes through strategies including morphological regulation and ionic doping, etc.,<sup>9–14</sup> the capacitance enhancement cannot meet the ever-increasing demand. Alternatively, transition metal nitrides are attractive candidates due to their excellent electrochemical performance and stability in mild electrolytes.<sup>11,15,16</sup> In this

regard, combining Zn and transition metal nitrides is expected to result in high-performance ZIHCs.

TiN has been widely explored for electrochemical energy storage applications given its high electrical conductivity (27 μΩ cm<sup>-1</sup>) and robust chemical/electrochemical stability.<sup>4,11</sup> However, the capacitance needs further improvement. On the other hand, vanadium-based materials have demonstrated excellent performance for batteries and supercapacitors thanks to multiple oxidation states of vanadium (V<sup>2+</sup>, V<sup>3+</sup>, V<sup>4+</sup>, V<sup>5+</sup>), while they have been suffering from unsatisfactory stability.<sup>13,17–20</sup> It is expected that the incorporation of vanadium into TiN might be a simple yet efficient way to optimize the overall performance with high capacitance and robust durability by utilizing the synergy between Ti and V.

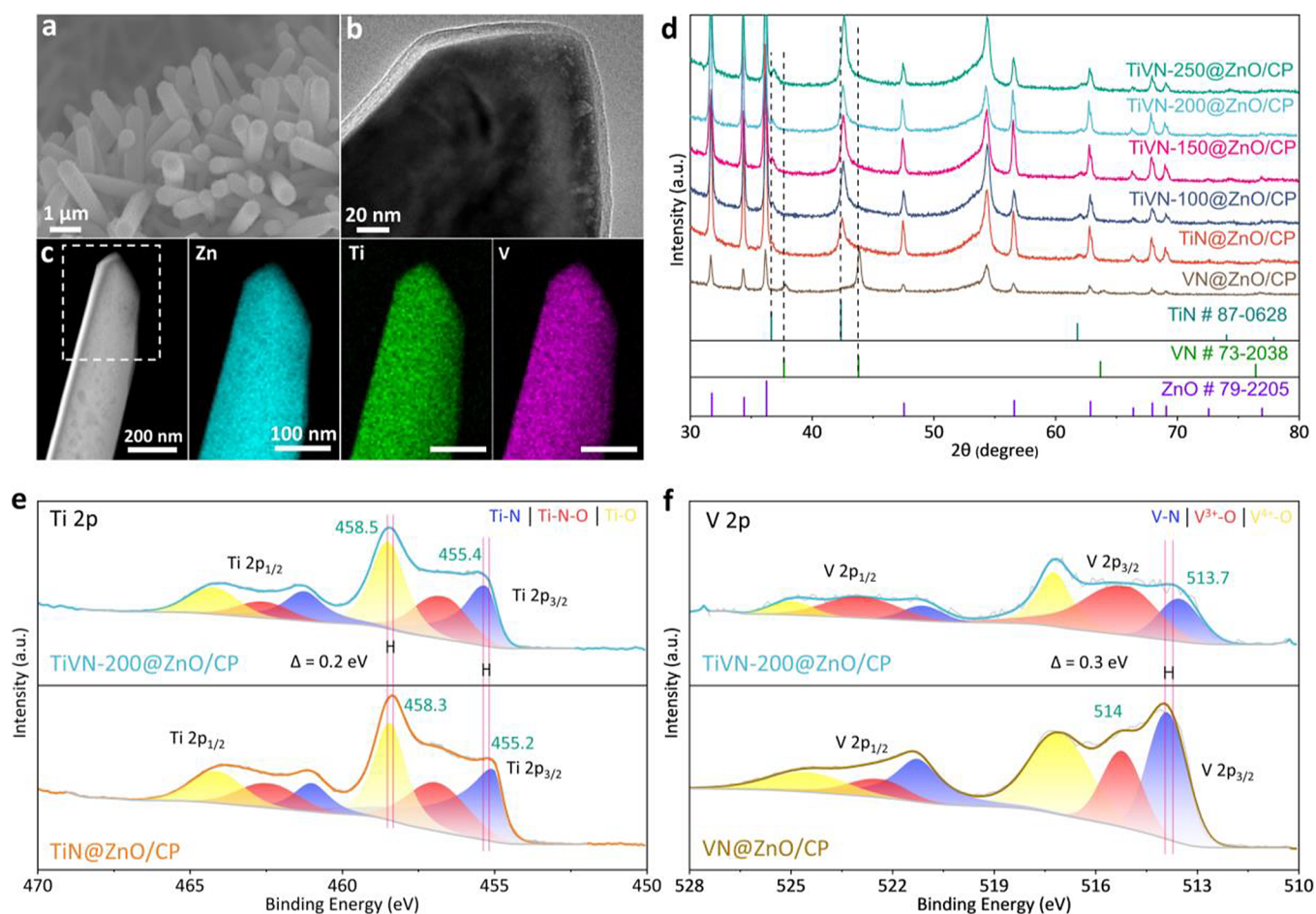


**Figure 1.** (a) SEM, (b) TEM, and (c) HAADF images and EDS elemental maps of TiVN-200@ZnO/CP. (d) XRD patterns and (e) Ti 2p and (f) V 2p XPS spectra of TiVN@ZnO/CP, TiN@ZnO/CP, and VN@ZnO/CP.

It is also noted that hollow structures typically have large surface areas and therefore would promote the contact between electrolyte and electrode, effectively enhancing mass transport and diffusion. In addition, the hollow structure also allows for better access to active sites and can alleviate the volume change during ion insertion/extraction. Therefore, hollow structures often possess enhanced capacity and stability compared to their solid counterparts. Indeed, many hollow structures of carbons have been explored for Zn-ion capacitors.<sup>21–25</sup> However, the synthesis of hollow nitrides with controlled compounds is much more challenging.

Herein, we proposed bimetallic TiVN as a promising cathode for ZIHC, and we further rationally designed a hollow TiVN nanostructure (H-TiVN) using ZnO nanorods as the sacrificial template to boost the ionic transfer and thus the electrochemical performance. The H-TiVN showed the best performance with a Ti/V ratio of 5.54. The H-TiVN//Zn hybrid capacitor can achieve a specific capacitance of 183.7 F g<sup>-1</sup> at 0.2 A g<sup>-1</sup>, which is far superior to that of a solid TiVN counterpart (62 F g<sup>-1</sup>). Additionally, the energy density can reach up to 57.42 Wh kg<sup>-1</sup>, accompanied by a high-power density of 249.35 W kg<sup>-1</sup>, and excellent stability with an 84.7% capacitance retention after 20,000 cycles at 5 A g<sup>-1</sup>. This work not only establishes H-TiVN as a high-performance electrode material that expands the potential applications of transition metal nitrides but also provides an effective strategy for

improving the electrochemical performance of nanomaterial electrodes by a combined compositional and structural design.

## RESULTS AND DISCUSSION

The TiVN was synthesized by magnetron sputtering, which is a common method used for large-scale synthesis of metal nitrides. However, materials produced by this technique often have a low surface area, leading to an unsatisfactory electrochemical performance. To address this, we introduced ZnO nanorods as a template and further deposited TiVN on the surface. The morphology of ZnO nanorod arrays was investigated by using SEM (Figure S1). TiVN@ZnO/CP samples with various Ti/V ratios were prepared by adjusting the RF power while maintaining the DC power at 150 W. The samples are denoted as TiVN-X (X = 100, 150, 200, or 250), where X represents the RF power. As control samples, we also prepared pure TiN and VN deposited on carbon paper (Table S1). SEM images reveal that the TiVN-X@ZnO/CP samples maintain the nanorod array's structure (Figures 1a and S2). Further observation by TEM (Figure 1b) confirms the core-shell structure of TiVN-X@ZnO, with a TiVN-X shell approximately 20 nm thick and a ZnO core approximately 200 nm in diameter. High-angle annular dark field SEM (HAADF) and energy dispersive spectroscopy (EDS) elemental mapping confirm the uniform distribution of Zn, Ti, V, and N elements (Figures 1c and S3). The Ti/V ratio of different TiVN-X@ZnO electrodes was determined by EDS

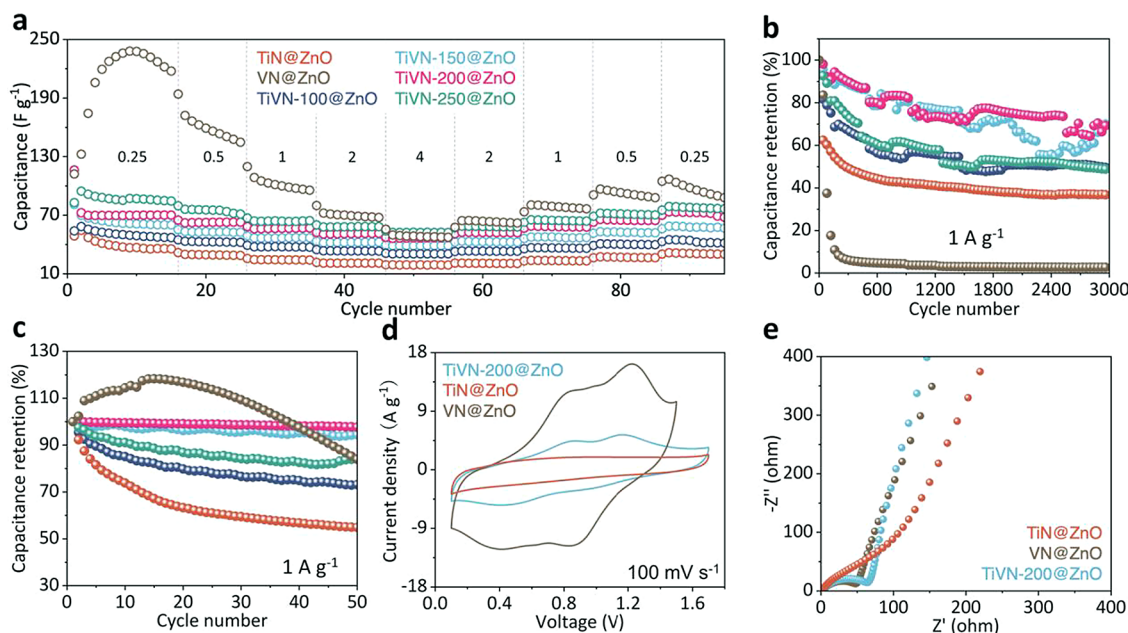


**Figure 2.** (a) Rate performance and (b,c) cycling performance of various electrodes of TiN@ZnO and VN@ZnO and various TiVN@ZnO electrodes. (d) CV curves at 100 mV s<sup>-1</sup> and (e) EIS spectra of the TiVN-200@ZnO/CP, TiN@ZnO/CP, and VN@ZnO/CP electrodes.

and is listed in Table S2. XRD patterns (Figure 1d) show clear ZnO diffraction peaks (JCPDS 79-2205) along with two additional peaks located at  $2\theta$  values of  $37^\circ$  and  $43^\circ$ . One peak ( $37^\circ$ ) is located between the (111) facet of TiN (JCPDS 87-0628) and VN (JCPDS 73-2038), while the other is located between the (200) facet of TiN and VN. The peaks shift to higher angles with increasing vanadium content, indicating the formation of Ti–V–N solid solutions.<sup>26,27</sup> Meanwhile, TiVN reveals a preferred (200) crystal plane orientation. The lattice parameter ( $a$ ) was determined using Bragg’s law and the plane-spacing equation as follows<sup>28</sup>:

$$a = d_{hkl}(h^2 + k^2 + l^2)^{1/2} \quad (1)$$

Taking TiVN-200@ZnO/CP as an example, the lattice parameter of TiVN was calculated to be 4.2 Å, compared to 4.244 Å for TiN and 4.13 Å for VN. This suggests that some Ti atoms (0.140 nm) are replaced by smaller V atoms (0.135 nm), further demonstrating the formation of Ti–V–N solid solutions. It should be noted that the variation of lattice parameters can also be attributed to the compressive stress generated during magnetron sputtering.<sup>29,30</sup>

XPS was performed to investigate the surface states. The Ti 2p peak fitting for TiVN-200@ZnO/CP can be divided into Ti–N (455.3 eV), Ti–N–O (456.8 eV), and Ti–O (458.5 eV) components.<sup>31,32</sup> Notably, these peaks shift by  $\sim 0.2$  eV toward higher binding energy compared to TiN@ZnO/CP, indicating electron deficiency (Figure 1e). For VN@ZnO/CP, the peaks at 513.9, 515.2, and 517.2 eV can be assigned to V–N, V<sup>3+</sup>–O, and V<sup>4+</sup>–O, respectively (Figure 1f). The V 2p peaks for the TiVN-200@ZnO/CP sample shift negatively by  $\sim 0.3$  eV, suggesting electronic interactions between V and Ti.<sup>33</sup> This could be due to the stronger electronegativity of V (1.63) attracting electrons from Ti, which has a weaker electronegativity (1.54). The N 1s spectrum of TiVN-200@ZnO/CP (Figure S4) further confirms the presence of V–N (396.3 eV), Ti–N (397.4 eV), Ti–N–O (398.5 eV), and V–O–N (399.5 eV) bonds.

We then evaluated the electrochemical performances of TiVN-X@ZnO/CP, TiN@ZnO/CP, and VN@ZnO/CP in 1 M Zn(SO<sub>4</sub>)<sub>2</sub> aqueous electrolyte. Figure S5 displays the CV curves at different scan rates. It is clear that as the content of V increases, the redox peaks become more distinct and a higher current response can be observed. Meanwhile, GCD curves confirm that the introduction of V leads to higher capacitance, which can be attributed to the contribution from V-related redox reactions (Figure S6).

Figure 2a–c shows the rate and stability performances of these electrodes. Generally, VN exhibits higher capacitance but suffers from rapid capacitance fading within 300 cycles. It is noted that there is an increase in the capacity of VN in the initial cycles, a phenomenon that has been commonly observed in the literature.<sup>34,35</sup> This process is mostly referred to as a so-called “activation process”, which is due to the oxidation of vanadium nitrides or chalcogenides and the consequent formation of amorphous vanadium oxides.<sup>36</sup> As for the TiVN, we did not observe such an “activation process”, which means that the oxidation of V species in TiVN to form vanadium oxides is somehow suppressed. Indeed, our XPS data indicates that there are strong electronic interactions between Ti and V in TiVN (Figure 1e,f), where the electrons are transferred from Ti to V. Therefore, although the initial capacity of TiVN is lower than that of VN, it surpasses the latter after long-term cycling. Among these samples, the TiVN-200@ZnO/CP demonstrated the best performance in terms of capacitance and stability and was therefore selected for the subsequent experiments. Figure 2d compares the CV curves of the TiVN-200@ZnO/CP, TiN@ZnO/CP, and VN@ZnO/CP electrodes at a scan rate of 100 mV s<sup>-1</sup>. The TiVN-200@ZnO/CP and VN@ZnO/CP electrodes exhibit typical redox peaks that are associated with the oxidation/reduction of V species.<sup>37</sup> The TiVN-200@ZnO/CP electrode delivers a higher current response than the TiN@ZnO/CP electrode without compromising the voltage window. The Nyquist plot reveals that TiVN-200@ZnO/CP exhibits better conductivity, faster charge transfer, and diffusion rates, as evidenced by the



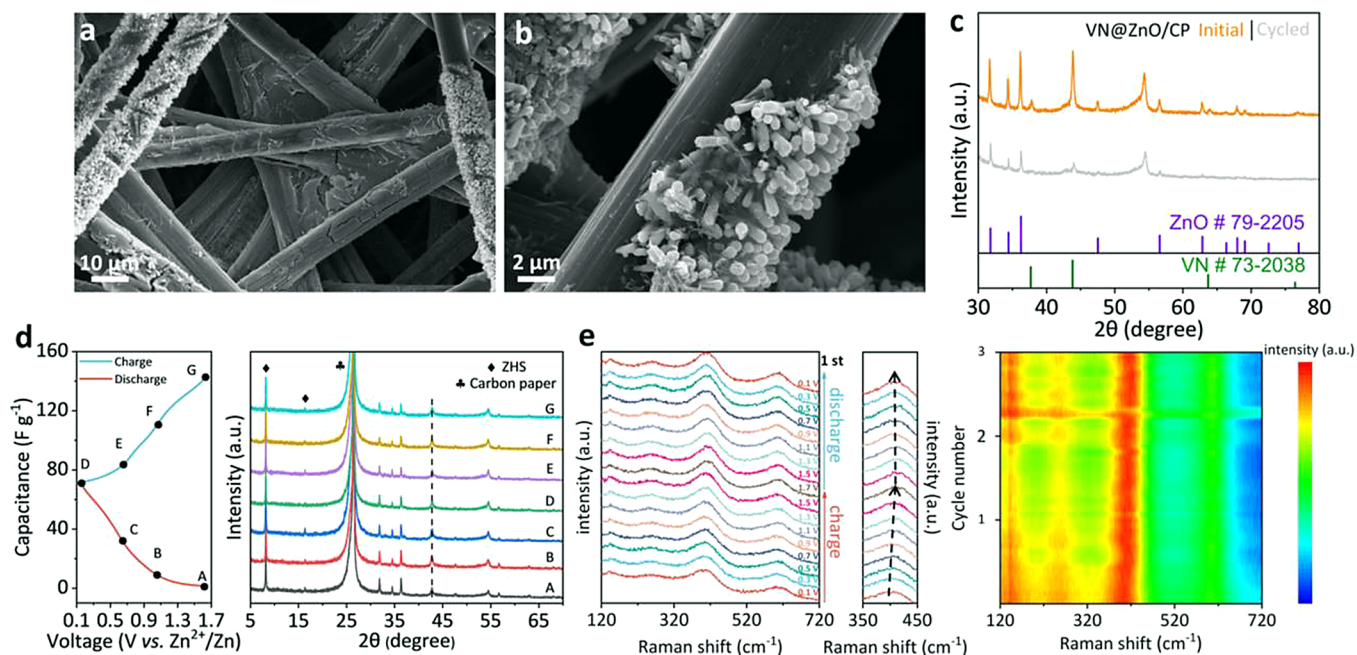


**Figure 3.** (a, b) SEM images of VN@ZnO/CP after 3000 cycles at 1 A g<sup>-1</sup>. (c) XRD patterns of the VN@ZnO/CP before and after cycling. (d) Ex situ XRD patterns, and (e) in situ Raman spectra of the TiVN-200@ZnO/CP electrode.

smaller intercept, radius of curvature, and larger straight slope (Figure 2e).

We hypothesize that the poor cycling stability of the VN@ZnO/CP electrode is due to the instability of ZnO and vanadium dissolution in acid environments.<sup>38–40</sup> We then conducted postcharacterizations of the electrode. SEM images reveal a significant structural collapse of the VN@ZnO/CP, indicating the dissolution of active materials (Figure 3a,b). XRD results further reveal the disappearance of the VN peaks and the weakened ZnO diffraction peaks (Figure 3c), confirming our hypothesis.

To understand the energy storage mechanism of the TiVN@ZnO/CP electrode, we conducted ex situ XRD (Figure 3d) and in situ Raman (Figure 3e) studies. These reveal the formation of zinc hydroxide sulfate (ZHS) during the charge/discharge process. Interestingly, no significant diffraction peak shift is observed (as indicated by the dashed lines in the figure), suggesting no major phase transformation throughout the process. The in situ Raman spectra of TiVN-200@ZnO/CP (Figure 3e) show peaks at 301 and 603 cm<sup>-1</sup> that can be assigned to ZnO, while peaks at 173 and 427 cm<sup>-1</sup> are ascribed to TiN. Two additional peaks at 130 and 400 cm<sup>-1</sup> deviate slightly from the standard TiN peak. We believe that this may be due to the introduction of V, which could extend the bond length of the Ti–V–N bonds, thereby reducing the bond energy of the Ti–N bonds and causing a redshift of the Raman peaks.<sup>16,41,42</sup> Meanwhile, a red shift of Raman peaks was also observed during the discharge process, possibly due to the reduction reaction that decreases the overall valence state and weakens the bond energy.

Nevertheless, the overall cycling stability and capacitance are still far from satisfactory. Given that ZnO does not contribute to the capacity and actually undermines the stability, we etched the ZnO template in 0.5 M HCl, resulting in the formation of H-TiVN/CP. SEM and TEM images (Figure 4) confirm the hollow structure and the nanorod array on carbon paper. The HRTEM image (Figure 4e) and the SAED pattern validate the

presence of (111) and (200) planes of TiVN. Furthermore, the high-angle annular dark field SEM (HAADF) and energy dispersive spectroscopy (EDS) elemental mapping (Figure 4g) confirm the uniform distribution of Ti, V, and N elements and the elimination of Zn (Figure S7). Line scanning of H-TiVN/CP revealed strong signals of Ti and V, indicating that the nanorod morphology is primarily composed of bimetallic nitride TiVN, with no significant signals of Zn observed. These results demonstrate successful removal of the ZnO template while maintaining the nanorod array structure. We then evaluated the performance of the H-TiVN/CP electrode and compared it with TiVN particles (P-TiVN/CP, the morphology is shown in Figure S8). Both electrodes exhibit obvious redox peaks, while the H-TiVN/CP shows a much higher current response owing to its rationally designed nanostructure, which provides a much higher specific surface area. The EIS spectra also confirm that H-TiVN/CP possesses better conductivity, faster charge transfer, and diffusion rate, leading to enhanced electrochemical performance (Figure S9).

To further analyze the reaction kinetics, we collected the CV curves at different scan rates (Figures 5a and S10) and calculated the *b* values according to the power law relationship between redox peak currents and scan rates:<sup>43</sup>

$$i_p = a\nu^b \quad (2)$$

where *i<sub>p</sub>* is the peak current (mA), *ν* is the sweep rate (mV s<sup>-1</sup>), and *a* and *b* are variables. A *b* value of 0.5 or 1 represents the diffusion- or capacitive-controlled behavior, respectively. The result reveals that the H-TiVN/CP electrode has higher *b* values of 0.91 and 0.77 than those of the TiVN/CP electrode, suggesting capacitive-dominated energy storage behavior (Figure 5b). This also ensures superior rate performance. Indeed, as the current density increases from 0.2 to 6.4 A g<sup>-1</sup>, the former displays a capacitance retention of 54.4% (from 183.7 to 99.9 F g<sup>-1</sup>), compared to 34.8% (from 79.5 to 27.7 F g<sup>-1</sup>) of the latter. Meanwhile, the contributions of capacitive-



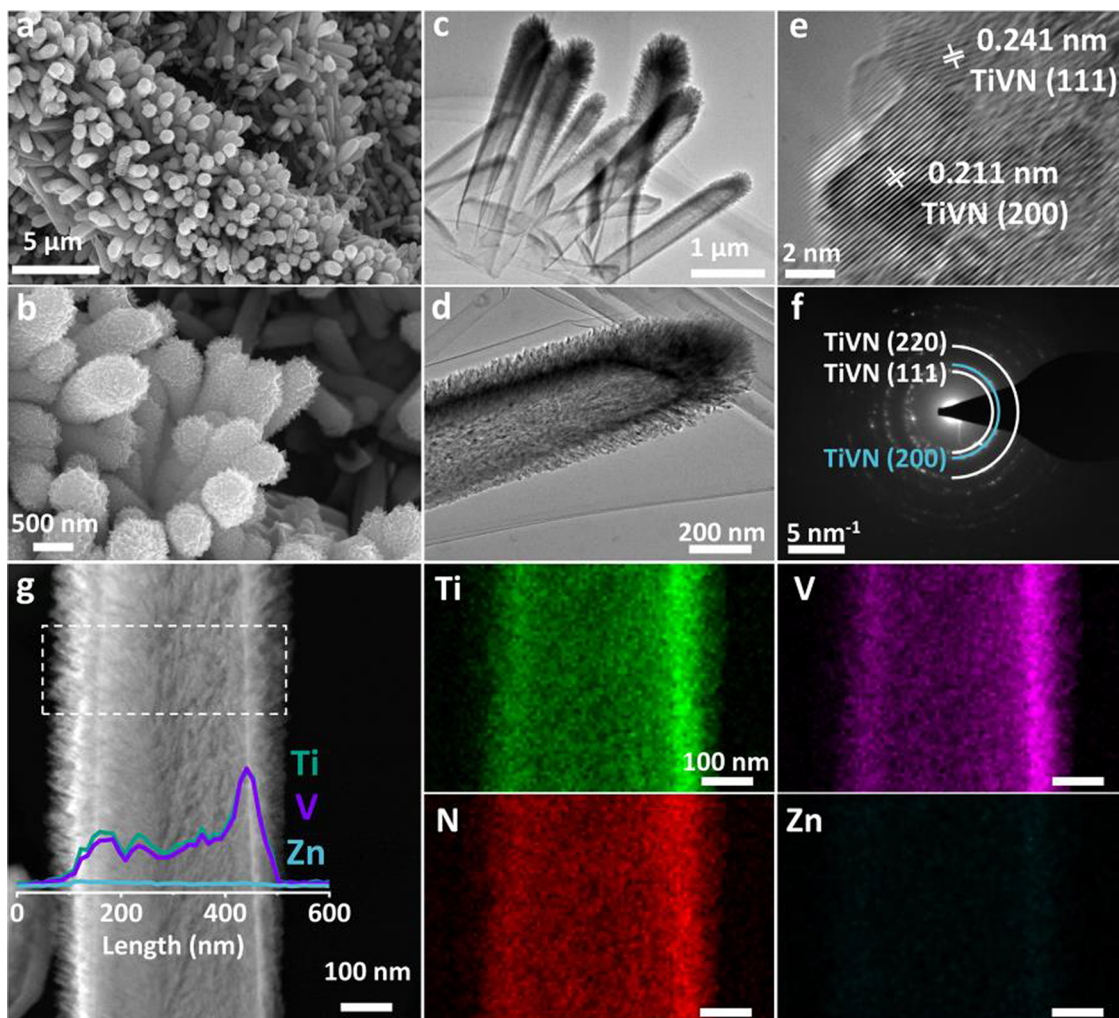


**Figure 4.** Morphological characterization of the H-TiVN/CP electrode. (a, b) SEM, (c, d) TEM, and (e) HRTEM image, (f) SAED pattern, and (g) HADDF image and EDS elemental maps.

controlled and diffusion-controlled performance can be further quantified according to the following equations<sup>37</sup>:

$$i_p = i_{\text{cap}} + i_{\text{dif}} = k_1\nu + k_2\nu^{1/2} \quad (3)$$

$$\frac{i_p}{\nu^{1/2}} = k_1\nu^{1/2} + k_2 \quad (4)$$

where  $i_{\text{cap}} = k_1\nu$  refers to the capacitive-controlled current, and  $i_{\text{dif}} = k_2\nu^{1/2}$  stands for the diffusion-controlled current.  $k_1$  and  $k_2$  can be calculated by the plot of  $\frac{i_p}{\nu^{1/2}}$  against  $k_1\nu^{1/2}$ . The result shows that the charge storage of the H-TiVN/CP is dominated by the capacitive-controlled behavior and is higher than that of the TiVN/CP electrode, which contributes from 55.7 to 79.65% at the scan rate range of 10–100 mV s<sup>-1</sup> (Figure 5c).

Significantly, the energy density can reach 57.42 Wh kg<sup>-1</sup> (based on the mass of the H-TiVN active material), accompanied by a power density of 249.35 W kg<sup>-1</sup>, which is potentially promising for ZIHCs (Figure 5e). The cycling stability was tested at a current density of 5 A g<sup>-1</sup> for 20,000 cycles. The H-TiVN/CP demonstrated a capacitance retention of 84.7%, which is superior to the 68.6% of the TiVN/CP electrode (Figure 5f). The enhanced electrochemical performance of H-TiVN/CP can be attributed to its two-dimensional

hollow nanorod structure, which provides a facile ion transport pathway, larger contact area, and shorter diffusion length. Figure Sg compares the cyclic stability of our H-TiVN/CP with previously reported materials. It clearly shows that the electrochemical performance and cycling durability of H-TiVN/CP surpass most of the reported materials, including H<sub>2</sub>Ti<sub>11.85</sub>Nb<sub>0.15</sub>O<sub>25</sub>//AC,<sup>44</sup> TWC//Zn,<sup>11</sup> GR/VN//GR/V<sub>2</sub>O<sub>5</sub>,<sup>45</sup> TiN//Zn,<sup>4</sup> Zn//AC,<sup>9</sup> MnO<sub>2</sub>//Zn,<sup>46</sup> Na<sub>0.11</sub>MnO<sub>2</sub>//Zn,<sup>47</sup> etc. (see more details in Table S3). Meanwhile, the SEM image and XRD pattern of H-TiVN/CP after cycling reveal no significant changes in the morphology and composition (Figure S11).

## CONCLUSIONS

In summary, we have developed a simple yet efficient strategy to significantly enhance the electrochemical performance of transition metal nitrides for zinc-ion hybrid supercapacitors. This strategy involves simultaneous composition and structure engineering. Using the widely explored TiN as a demonstration, we showed that the incorporation of V enriches the redox chemistry; by further creating hollow nanostructures, we can greatly boost the electrochemical performance. Specifically, the optimized H-TiVN/CP//Zn device exhibits a high capacitance of 183.7 F g<sup>-1</sup> at 0.2 A g<sup>-1</sup> and outstanding

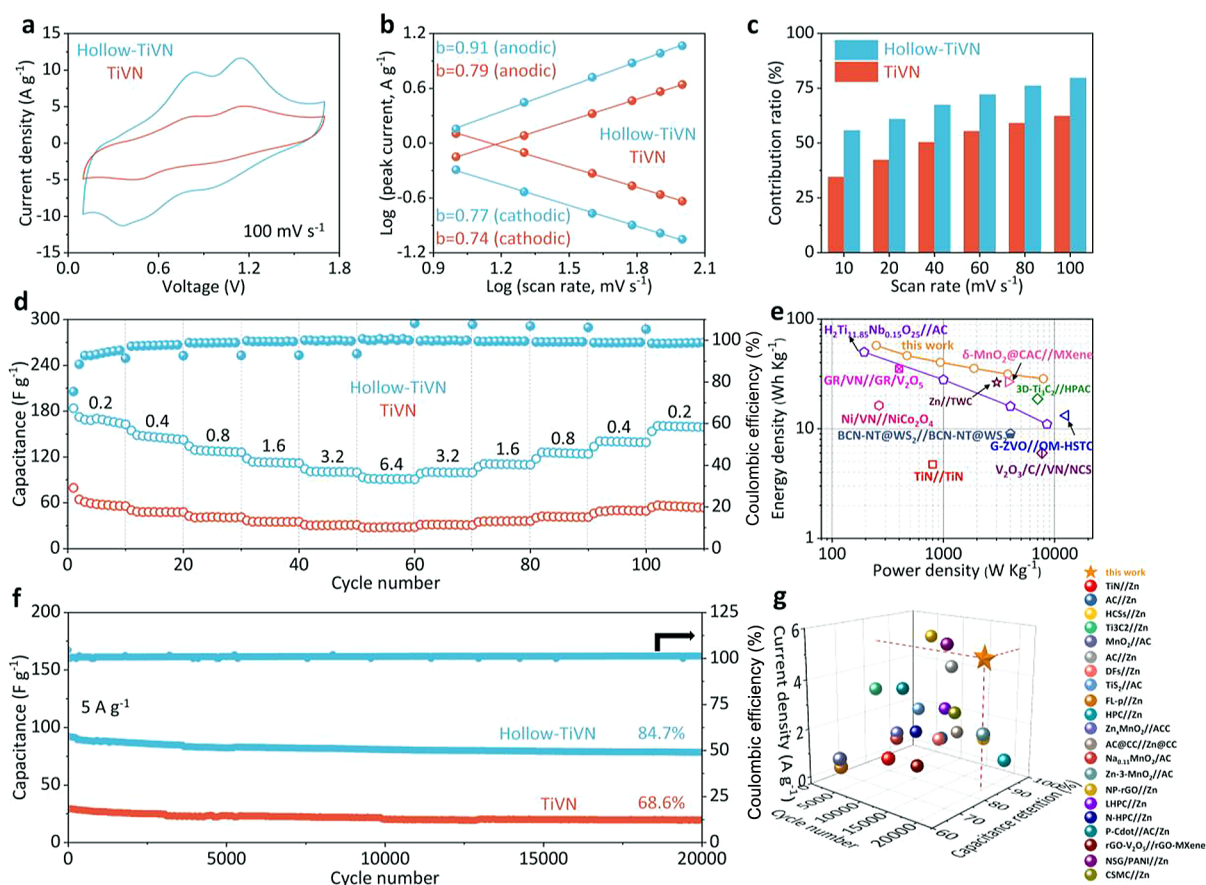


**Figure 5.** (a) CV curves, (b)  $\log(i_p)$  versus  $\log(\nu)$  plots, (c) contribution ratio of capacitive-controlled behavior at different scan rates, and (d) rate performance of the TiVN/CP and H-TiVN/CP electrodes. (e) Ragone plots of the H-TiVN/CP//Zn ASC and other zinc-ion hybrid supercapacitors. (f) Capacitance retention and Coulombic efficiency versus cycle number at 5 A g<sup>-1</sup> for 20,000 cycles, and (g) performance comparison of H-TiVN/CP//Zn ASC with other reported hybrid supercapacitors.

cycling stability with an 84.7% capacitance retention over 20,000 cycles at 5 A g<sup>-1</sup>. More importantly, the H-TiVN/CP//Zn device reveals a high energy density of 57.42 Wh kg<sup>-1</sup> at a power density of 249.35 W kg<sup>-1</sup>. This effective strategy holds potential as a universal method to improve the electrochemical performance of other electrode materials.

## METHODS

**Preparation of ZnO Nanorod Arrays on Carbon Paper (ZnO/CP).** The carbon paper (CP, 3 cm × 3 cm) was ultrasonically cleaned for 20 min in acetone, deionized water, and ethanol, respectively, and then dried at 60 °C. Then, it was soaked in 0.5 M KMnO<sub>4</sub> solution for 2 h to complete the hydrophilic treatment. The ZnO nanorods on CP were obtained by hydrothermally reacting 0.2231 g of Zn(NO<sub>3</sub>)<sub>2</sub>·6H<sub>2</sub>O with 0.1051 g of HMTA along with 2 mL of ammonia–water in a 50 mL Teflon-lined stainless-steel autoclave at 85 °C for 24 h. The mass loading of ZnO/CP was ~2 mg cm<sup>-2</sup>.

**Preparation of TiVN@ZnO on Carbon Paper (TiVN@ZnO/CP).** The TiVN@ZnO/CP was obtained by direct current (DC) and radio frequency (RF) reactive magnetron cosputtering TiVN onto ZnO/CP. Pure Ti (99.95%) and V (99.9%) metal targets were used in a mixed atmosphere of Ar and N<sub>2</sub> (>99.999% purity with a total flux of 60 sccm, 9% N<sub>2</sub>). The distance between the target and the substrate was 10 cm. The chamber temperature and the substrate temperature were heated to 120 and 200 °C, respectively. Before deposition, the substrate was presputtered by Ar<sup>+</sup> bombardment under 1.0 Pa with a bias voltage of 100 V for 2 min. During sputtering, the pressure was maintained at 1.0 Pa, and the DC power of the Ti target was kept at 150 W for 45 min. The Ti/V ratio of the electrode was regulated by changing the RF power of the V target. TiVN was

directly sputtered on pure carbon paper as a control sample (TiVN/CP). The typical mass loading of TiVN@ZnO/CP was ~2.4 mg cm<sup>-2</sup>.

### Preparation of Hollow-TiVN on Carbon Paper (H-TiVN/CP).

The prepared TiVN@ZnO/CP was immersed in 0.5 M HCl for 30 min, and then the ZnO was etched away to obtain the H-TiVN/CP electrode, which was rinsed using deionized water and dried in a vacuum. The typical mass loading of H-TiVN/CP was ~0.35 mg cm<sup>-2</sup>.

**Material Characterization.** A ZEISS SIGMA scanning electron microscope (SEM) was used to observe the surface structure and morphology of the electrode materials. The crystal structure and composition of the electrode materials were characterized by X-ray photoelectron spectroscopy (XPS, PHI-Quantum-2000) with Al K $\alpha$  radiation and X-ray diffraction (XRD, Rigaku X-ray) with Cu K $\alpha$  radiation. Raman spectra were recorded on a LabRAM HR laser spectroscopy. The further study of the structure and elemental distribution were obtained by transmission electron microscopy (TEM) and high-resolution TEM (HRTEM) images, as well as the energy dispersive spectrometer (EDS) spectra, which were collected on an FEI Talos F200x microscope at an acceleration voltage of 200 kV.

**Electrochemical Measurements.** All electrochemical measurements of individual electrodes were conducted in a 1 M Zn(SO<sub>4</sub>)<sub>2</sub> electrolyte with an electrochemical workstation (CHI 760E) in a two-electrode configuration. The as-obtained materials on CP served as the positive electrode, and Zn foil served as the negative electrode. Meanwhile, the ZIHs were assembled as coin cells. Cyclic voltammetry (CV), galvanostatic charge–discharge (GCD), and electrochemical impedance spectroscopy (EIS, 10 mV to 100 kHz

at the open circuit potential) were used to analyze electrochemical performance. The specific gravimetric capacity ( $F \text{ g}^{-1}$ ) was calculated from the GCD curves as following:

$$C_m = \frac{2I \int V(t)dt}{MV^2} \quad (5)$$

where  $I$  (mA) is the constant current,  $V$  (V) is the voltage window,  $t$  (s) is the discharge time, and  $M$  (mg) is the mass of the active materials on the substrate, respectively.

The power density ( $P$ ,  $W \text{ kg}^{-1}$ ) and energy density ( $E$ ,  $Wh \text{ kg}^{-1}$ ) were calculated from the GCD curves as follows:

$$E = \frac{I \int V(t)dt}{3600M_{vol}} \quad (6)$$

$$P = \frac{3600E}{t} \quad (7)$$


where  $M_{vol}$  (mg) is the total mass of the active material.

## AUTHOR INFORMATION

### Corresponding Authors

**Huanhuan Shi** – Institut für Quanten Materialien and Technologien (IQMT), Karlsruhe Institut für Technologie (KIT), 76131 Karlsruhe, Germany; Email: [huanhuan.shi@kit.edu](mailto:huanhuan.shi@kit.edu)

**Fangwang Ming** – Materials Science and Engineering, King Abdullah University of Science and Technology, Thuwal 23955, Saudi Arabia;  [orcid.org/0000-0003-4574-9720](https://orcid.org/0000-0003-4574-9720); Email: [fangwang.ming@kaust.edu.sa](mailto:fangwang.ming@kaust.edu.sa)

**Hanfeng Liang** – State Key Laboratory of Physical Chemistry of Solid Surfaces, Tan Kah Kee Innovation Laboratory, College of Chemistry and Chemical Engineering, Xiamen University, Xiamen 361005, China;  [orcid.org/0000-0002-1778-3975](https://orcid.org/0000-0002-1778-3975); Email: [hfliang@xmu.edu.cn](mailto:hfliang@xmu.edu.cn)

### Authors

**Hao Zhou** – State Key Laboratory of Physical Chemistry of Solid Surfaces, Tan Kah Kee Innovation Laboratory, College of Chemistry and Chemical Engineering, Xiamen University, Xiamen 361005, China

**Zhilong Zheng** – State Key Laboratory of Physical Chemistry of Solid Surfaces, Tan Kah Kee Innovation Laboratory, College of Chemistry and Chemical Engineering, Xiamen University, Xiamen 361005, China

**Jiaxian Zheng** – State Key Laboratory of Physical Chemistry of Solid Surfaces, Tan Kah Kee Innovation Laboratory, College of Chemistry and Chemical Engineering, Xiamen University, Xiamen 361005, China

**Yuwei Zhang** – State Key Laboratory of Physical Chemistry of Solid Surfaces, Tan Kah Kee Innovation Laboratory, College of Chemistry and Chemical Engineering, Xiamen University, Xiamen 361005, China

**Weijie Zhu** – State Key Laboratory of Physical Chemistry of Solid Surfaces, Tan Kah Kee Innovation Laboratory, College

of Chemistry and Chemical Engineering, Xiamen University, Xiamen 361005, China

**Zhoucheng Wang** – State Key Laboratory of Physical Chemistry of Solid Surfaces, Tan Kah Kee Innovation Laboratory, College of Chemistry and Chemical Engineering, Xiamen University, Xiamen 361005, China

## Notes

The authors declare no competing financial interest.

## ACKNOWLEDGMENTS

This work was supported by the National Natural Science Foundation of China (Grant No.: 22075236 and 22001081) and the Science and Technology Projects of Innovation Laboratory for Sciences and Technologies of Energy Materials of Fujian Province (IKKEM, Grant No.: H RTP-[2022]-7).

## REFERENCES

- (1) Wang, Y.; Sun, S.; Wu, X.; Liang, H.; Zhang, W. Status and Opportunities of Zinc Ion Hybrid Capacitors: Focus on Carbon Materials, Current Collectors, and Separators. *Nano-Micro Lett.* **2023**, *15* (1), 78.
- (2) Liu, X.; Sun, Y.; Tong, Y.; Wang, X.; Zheng, J.; Wu, Y.; Li, H.; Niu, L.; Hou, Y. Exploration in Materials, Electrolytes and Performance Towards Metal Ion (Li, Na, K, Zn and Mg)-Based Hybrid Capacitors: A Review. *Nano Energy* **2021**, *86*, No. 106070.
- (3) Naskar, P.; Kundu, D.; Maiti, A.; Chakraborty, P.; Biswas, B.; Banerjee, A. Frontiers in Hybrid Ion Capacitors: A Review on Advanced Materials and Emerging Devices. *ChemElectroChem.* **2021**, *8* (8), 1393–1429.
- (4) Huang, Z.; Wang, T.; Song, H.; Li, X.; Liang, G.; Wang, D.; Yang, Q.; Chen, Z.; Ma, L.; Liu, Z.; Gao, B.; Fan, J.; Zhi, C. Effects of Anion Carriers on Capacitance and Self-Discharge Behaviors of Zinc Ion Capacitors. *Angew. Chem., Int. Ed.* **2021**, *60* (2), 1011–1021.
- (5) Jian, Z.; Yang, N.; Vogel, M.; Leith, S.; Schulte, A.; Schönherr, H.; Jiao, T.; Zhang, W.; Müller, J.; Butz, B.; Jiang, X. Flexible Diamond Fibers for High-Energy-Density Zinc-Ion Supercapacitors. *Adv. Energy Mater.* **2020**, *10* (44), No. 2002202.
- (6) Su, L.; Liu, L.; Wang, Y.; Lu, Y.; Yan, X. Synergetic Ternary Metal Oxide Nanodots-Graphene Cathode for High Performance Zinc Energy Storage. *Chin. Chem. Lett.* **2020**, *31* (9), 2358–2364.
- (7) Jia, X.; Liu, C.; Neale, Z. G.; Yang, J.; Cao, G. Active Materials for Aqueous Zinc Ion Batteries: Synthesis, Crystal Structure, Morphology, and Electrochemistry. *Chem. Rev.* **2020**, *120* (15), 7795–7866.
- (8) Sun, G.; Yang, H.; Zhang, G.; Gao, J.; Jin, X.; Zhao, Y.; Jiang, L.; Qu, L. A Capacity Recoverable Zinc-Ion Micro-Supercapacitor. *Energy Environ. Sci.* **2018**, *11* (12), 3367–3374.
- (9) Chen, S.; Ma, L.; Zhang, K.; Kamruzzaman, M.; Zhi, C.; Zapfen, J. A. A Flexible Solid-State Zinc Ion Hybrid Supercapacitor Based on Co-Polymer Derived Hollow Carbon Spheres. *J. Mater. Chem. A* **2019**, *7* (13), 7784–7790.
- (10) Dong, L.; Ma, X.; Li, Y.; Zhao, L.; Liu, W.; Cheng, J.; Xu, C.; Li, B.; Yang, Q.-H.; Kang, F. Extremely Safe, High-Rate and Ultralong-Life Zinc-Ion Hybrid Supercapacitors. *Energy Stor. Mater.* **2018**, *13*, 96–102.
- (11) Wang, H.; Huang, J.; Wang, X.; Guo, Z.; Liu, W. Fabrication of TiN/CNTs on Carbon Cloth Substrates via a CVD-ALD Method as Free-Standing Electrodes for Zinc Ion Hybrid Capacitors. *New J. Chem.* **2022**, *46* (31), 15175–15184.
- (12) Yoon, K. R.; Shin, K.; Park, J.; Cho, S.-H.; Kim, C.; Jung, J.-W.; Cheong, J. Y.; Byon, H. R.; Lee, H. M.; Kim, I.-D. Brush-Like Cobalt Nitride Anchored Carbon Nanofiber Membrane: Current Collector-



Catalyst Integrated Cathode for Long Cycle Li–O<sub>2</sub> Batteries. *ACS Nano* **2018**, *12* (1), 128–139.

(13) Ren, W.; Xu, L.; Zhu, L.; Wang, X.; Ma, X.; Wang, D. Cobalt-Doped Vanadium Nitride Yolk–Shell Nanospheres @ Carbon with Physical and Chemical Synergistic Effects for Advanced Li–S Batteries. *ACS Appl. Mater. Interfaces* **2018**, *10* (14), 11642–11651.

(14) Simon, P.; Gogotsi, Y. Capacitive Energy Storage in Nanostructured Carbon-Electrolyte Systems. *Acc. Chem. Res.* **2013**, *46* (5), 1094–1103.

(15) Wei, B.; Liang, H.; Qi, Z.; Zhang, D.; Shen, H.; Hu, W.; Wang, Z. Construction of 3D Si@Ti@TiN Thin Film Arrays for Aqueous Symmetric Supercapacitors. *Chem. Commun.* **2019**, *55* (10), 1402–1405.

(16) Zhao, F.; Xue, X.; Fu, W.; Liu, Y.; Ling, Y.; Zhang, Z. TiN Nanorods as Effective Substrate for Surface-Enhanced Raman Scattering. *J. Phys. Chem. C* **2019**, *123* (48), 29353–29359.

(17) Wan, F.; Niu, Z. Design Strategies for Vanadium-Based Aqueous Zinc-Ion Batteries. *Angew. Chem., Int. Ed.* **2019**, *58* (46), 16358–16367.

(18) Hu, P.; Yan, M.; Zhu, T.; Wang, X.; Wei, X.; Li, J.; Zhou, L.; Li, Z.; Chen, L.; Mai, L. Zn/V<sub>2</sub>O<sub>5</sub> Aqueous Hybrid-Ion Battery with High Voltage Platform and Long Cycle Life. *ACS Appl. Mater. Interfaces* **2017**, *9* (49), 42717–42722.

(19) Du, M.; Liu, C.; Zhang, F.; Dong, W.; Zhang, X.; Sang, Y.; Wang, J.-J.; Guo, Y.-G.; Liu, H.; Wang, S. Tunable Layered (Na,Mn)V<sub>8</sub>O<sub>20</sub>·nH<sub>2</sub>O Cathode Material for High-Performance Aqueous Zinc Ion Batteries. *Adv. Sci.* **2020**, *7* (13), No. 2000083.

(20) Guo, J.; Zhang, Q.; Li, Q.; Sun, J.; Li, C.; He, B.; Zhou, Z.; Xie, L.; Li, M.; Yao, Y. Rational Design of Hierarchical Titanium Nitride@Vanadium Pentoxide Core–Shell Heterostructure Fibrous Electrodes for High-Performance 1.6 V Nonpolarity Wearable Supercapacitors. *ACS Appl. Mater. Interfaces* **2018**, *10* (35), 29705–29711.

(21) Liu, P.; Liu, W.; Huang, Y.; Li, P.; Yan, J.; Liu, K. Mesoporous Hollow Carbon Spheres Boosted, Integrated High Performance Aqueous Zn-Ion Energy Storage. *Energy Stor. Mater.* **2020**, *25*, 858–865.

(22) Li, J.; Zhang, J.; Yu, L.; Gao, J.; He, X.; Liu, H.; Guo, Y.; Zhang, G. Dual-Doped Carbon Hollow Nanospheres Achieve Boosted Pseudocapacitive Energy Storage for Aqueous Zinc Ion Hybrid Capacitors. *Energy Stor. Mater.* **2021**, *42*, 705–714.

(23) Fei, R.; Wang, H.; Wang, Q.; Qiu, R.; Tang, S.; Wang, R.; He, B.; Gong, Y.; Fan, H. J. In Situ Hard-Template Synthesis of Hollow Bowl-Like Carbon: A Potential Versatile Platform for Sodium and Zinc Ion Capacitors. *Adv. Energy Mater.* **2020**, *10* (47), No. 2002741.

(24) Cao, Y.; Tang, X.; Liu, M.; Zhang, Y.; Yang, T.; Yang, Z.; Yu, Y.; Li, Y.; Di, J.; Li, Q. Thin-Walled Porous Carbon Tile-Packed Paper for High-Rate Zn-Ion Capacitor Cathode. *Chem. Eng. J.* **2022**, *431*, No. 133241.

(25) Zhang, Y.; Zhu, C.; Xiong, Y.; Gao, Z.; Hu, W.; Shi, J.; Chen, J.; Tian, W.; Wu, J.; Huang, M. Multi-Channel Hollow Carbon Nanofibers with Graphene-Like Shell-Structure and Ultrahigh Surface Area for High-Performance Zn-Ion Hybrid Capacitors. *Small Methods* **2023**, *7* (11), No. 2300714.

(26) Schmitt, R.; Nenning, A.; Kraynis, O.; Korobko, R.; Frenkel, A. I.; Lubomirsky, I.; Haile, S. M.; Rupp, J. L. M. A Review of Defect Structure and Chemistry in Ceria and Its Solid Solutions. *Chem. Soc. Rev.* **2020**, *49* (2), 554–592.

(27) Pinto, D.; Anasori, B.; Avireddy, H.; Shuck, C. E.; Hantanasirisakul, K.; Deysher, G.; Morante, J. R.; Porzio, W.; Alshareef, H. N.; Gogotsi, Y. Synthesis and Electrochemical Properties of 2D Molybdenum Vanadium Carbides – Solid Solution Mxenes. *J. Mater. Chem. A* **2020**, *8* (18), 8957–8968.

(28) Anusha Thampi, V. V.; Nithiyantham, U.; Nanda Kumar, A. K.; Martin, P.; Bendavid, A.; Subramanian, B. Fabrication of Sputtered Titanium Vanadium Nitride (TiVN) Thin Films for Micro-Supercapacitors. *J. Mater. Sci.* **2018**, *29* (14), 12457–12465.

(29) Hanumantha, P. J.; Datta, M. K.; Kadakia, K. S.; Hong, D. H.; Chung, S. J.; Tam, M. C.; Poston, J. A.; Manivannan, A.; Kumta, P. N. A Simple Low Temperature Synthesis of Nanostructured Vanadium

Nitride for Supercapacitor Applications. *J. Electrochem. Soc.* **2013**, *160* (11), A2195.

(30) Avasara, B.; Haldar, P. Electrochemical Oxidation Behavior of Titanium Nitride Based Electrocatalysts under Pem Fuel Cell Conditions. *Electrochim. Acta* **2010**, *55* (28), 9024–9034.

(31) Yang, P.; Chao, D.; Zhu, C.; Xia, X.; Zhang, Y.; Wang, X.; Sun, P.; Tay, B. K.; Shen, Z. X.; Mai, W.; Fan, H. J. Ultrafast-Charging Supercapacitors Based on Corn-Like Titanium Nitride Nanostructures. *Adv. Sci.* **2016**, *3* (6), No. 1500299.

(32) Achour, A.; Lucio-Porto, R.; Chaker, M.; Arman, A.; Ahmadpourian, A.; Soussou, M. A.; Boujtita, M.; Le Brizoul, L.; Djouadi, M. A.; Brousse, T. Titanium Vanadium Nitride Electrode for Micro-Supercapacitors. *Electrochem. Commun.* **2017**, *77*, 40–43.

(33) Zeng, Y.; Liao, J.; Wei, B.; Huang, Z.; Zhu, W.; Zheng, J.; Liang, H.; Zhang, Y.; Wang, Z. Tuning the Electronic Structure of NiMoO<sub>4</sub> by Coupling with SnO<sub>2</sub> for High-Performance Hybrid Supercapacitors. *Chem. Eng. J.* **2021**, *409*, No. 128297.

(34) Chen, H.; Yang, Z.; Wu, J.; Rong, Y.; Deng, L. Industrial VN@Reduced Graphene Oxide Cathode for Aqueous Zinc Ion Batteries with High Rate Capability and Long Cycle Stability. *J. Power Sources* **2021**, *507*, No. 230286.

(35) Du, W.; Miao, L.; Song, Z.; Zheng, X.; Lv, Y.; Zhu, D.; Gan, L.; Liu, M. Kinetics-Driven Design of 3D VN/Mxene Composite Structure for Superior Zinc Storage and Charge Transfer. *J. Power Sources* **2022**, *536*, No. 231512.

(36) Zhang, S.; Liu, Z.; Li, L.; Tang, Y.; Li, S.; Huang, H.; Zhang, H. Electrochemical Activation Strategies of a Novel High Entropy Amorphous V-Based Cathode Material for High-Performance Aqueous Zinc-Ion Batteries. *J. Mater. Chem. A* **2021**, *9* (34), 18488–18497.

(37) Zhou, H.; Alam, M.; Wu, Y.; Zeng, Y.; Gandi, A. N.; Zheng, J.; Zhu, W.; Wang, Z.; Liang, H. Synergy of VN and Fe<sub>2</sub>O<sub>3</sub> Enables High Performance Anodes for Asymmetric Supercapacitors. *ACS Appl. Mater. Interfaces* **2023**, *15* (15), 18819–18827.

(38) Liu, H.; Jiang, L.; Cao, B.; Du, H.; Lu, H.; Ma, Y.; Wang, H.; Guo, H.; Huang, Q.; Xu, B. Van Der Waals Interaction-Driven Self-Assembly of V<sub>2</sub>O<sub>5</sub> Nanoplates and Mxene for High-Performing Zinc-Ion Batteries by Suppressing Vanadium Dissolution. *ACS Nano* **2022**, *16* (9), 14539–14548.

(39) Wei, Z.; Wang, X.; Zhu, T.; Hu, P.; Mai, L.; Zhou, L. Mitigating the Dissolution of V<sub>2</sub>O<sub>5</sub> in Aqueous ZnSO<sub>4</sub> Electrolyte through Ti-Doping for Zinc Storage. *Chin. Chem. Lett.* **2024**, *35* (1), No. 108421.

(40) Dai, Y.; Zhang, C.; Li, J.; Gao, X.; Hu, P.; Ye, C.; He, H.; Zhu, J.; Zhang, W.; Chen, R. Inhibition of Vanadium Cathodes Dissolution in Aqueous Zn-Ion Batteries. *Adv. Mater.* **2024**, *36*, No. e2310645.

(41) Akyil, C.; Akdaş, G.; Afşin, P.; Urgan, M. Freestanding SnO<sub>2</sub> Films Produced with Anodic Polarization in Acidic Media Containing Colloidal Tin Hydroxides. *Mater. Chem. Phys.* **2018**, *221*, 263 DOI: 10.1016/j.matchemphys.2018.09.062.

(42) Zhang, J.; Jiang, F.; Yang, Y.; Sui, C. Fabrication of ZnO:Ni Nanowires and Their Raman Spectra. *Mater. Lett.* **2017**, *195*, 136–138.

(43) Rahmanifar, M. S.; Hesari, H.; Noori, A.; Masoomi, M. Y.; Morsali, A.; Mousavi, M. F. A Dual Ni/Co-MOF-Reduced Graphene Oxide Nanocomposite as a High Performance Supercapacitor Electrode Material. *Electrochim. Acta* **2018**, *275*, 76–86.

(44) Lee, J. H.; Kim, H.-K.; Baek, E.; Pecht, M.; Lee, S.-H.; Lee, Y.-H. Improved Performance of Cylindrical Hybrid Supercapacitor Using Activated Carbon/Niobium Doped Hydrogen Titanate. *J. Power Sources* **2016**, *301*, 348–354.

(45) Deng, L.; Gao, Y.; Ma, Z.; Fan, G. Free-Standing Graphene/Vanadium Oxide Composite as Binder-Free Electrode for Asymmetrical Supercapacitor. *J. Colloid Interface Sci.* **2017**, *505*, 556–565.

(46) Ma, X.; Cheng, J.; Dong, L.; Liu, W.; Mou, J.; Zhao, L.; Wang, J.; Ren, D.; Wu, J.; Xu, C.; Kang, F. Multivalent Ion Storage Towards High-Performance Aqueous Zinc-Ion Hybrid Supercapacitors. *Energy Stor. Mater.* **2019**, *20*, 335–342.

(47) Ren, H.; Zhang, L.; Zhang, J.; Miao, T.; Yuan, R.; Chen, W.; Wang, Z.; Yang, J.; Zhao, B. Na<sup>+</sup> Pre-Intercalated Na<sub>0.11</sub>MnO<sub>2</sub> on

Three-Dimensional Graphene as Cathode for Aqueous Zinc Ion Hybrid Supercapacitor with High Energy Density. *Carbon* **2022**, 198, 46–56.